applied sciences

MDPI

Article

Space Object and Background Polarization Models and Detectability Analysis

Qiang Fu [1,2,*], Feng Zhao [1,2], Hongyi Chen [1,2], Rui Zhu [1,2] and Yingchao Li [1,2]

[1] Institute of Space Optoelectronics Technology, Changchun University of Science and Technology, Changchun 130022, China
[2] School of Opto-Electronic Engineering, Changchun University of Science and Technology, Changchun 130022, China
* Correspondence: cust_fuqiang@163.com

Abstract: During the daytime, the commonly used optical intensity imaging techniques for spacecraft detection usually lead to poor detection due to strong background noise. Since some materials with low reflectivity in the visible band have higher reflectivity in the near-infrared band and less sky background noise, this paper carries out a study of near-infrared polarization detection techniques. In this paper, firstly, the parameters in the pBRDF model of common materials are inverted and found to be improved compared with the literature, and secondly, a complex spherical projection is proposed to represent the polarization degree and polarization angle information of the sky background, and this projection has less aberration than the direct projection. Finally, from the above, the polarization detection contrast range and the original intensity contrast range are calculated, and it is found that the maximum of the former is higher than the latter in some angles.

Keywords: micro polarizer imaging; polarization bidirectional reflection distribution function; ground-based optical detection; complex spherical mapping

Citation: Fu, Q.; Zhao, F.; Chen, H.; Zhu, R.; Li, Y. Space Object and Background Polarization Models and Detectability Analysis. *Appl. Sci.* **2022**, *12*, 10714. https://doi.org/10.3390/app122110714

Academic Editor: Edik U. Rafailov

Received: 25 September 2022
Accepted: 19 October 2022
Published: 22 October 2022

1. Introduction

As the ground-to-earth reconnaissance capabilities of satellites in orbit increase [1–5], ground-based exploration of such satellites is required. The background noise is low and the contrast is strong when detecting at night, but it is difficult to increase these parameters during the day due to the influence of sunlight. Polarization detection has the advantage of enhancing the target to increase contrast, penetrating the haze to improve detection, and assisting in the extraction of the target information from the daytime noise. Any target will produce a distinctive polarization that is dictated by its own qualities in the process of reflection, scattering, and electromagnetic radiation. Space objects reflect sunlight to a high degree of polarization. This demonstrates that the surface polarization properties of the space object play a significant role in the target's identification. The Salfer Grove Observatory in Ohio, USA, installed a polarization device on the photoelectric detection telescope and used this technique to detect that the polarization degree of a satellite can reach a peak of 39% at a specific time, which was carried out in order to complete a series of polarization detection experiments on space targets.

The polarization degree is around 10% when the illumination signal is strong, but can reach 40% when the light characteristics of dawn are weak, according to a number of studies by Sanchez, which have demonstrated how the target's radiation characteristics and polarization characteristics differ significantly [6]. At the White Sand Range in 2011, the US military tested air-to-air polarization imaging for target tracking; as a result, the false alarm rate decreased from 0.52 to 0.01 [7]. Israel conducted polarization imaging studies in a hazy environment in 2005 [8]. The findings of the research demonstrated that polarization imaging might enhance picture contrast and broaden the scope of action.

Only at night can visible light intensity be detected, and during the day it is challenging to separate target information from noise. In order for the device to detect the target during the day, the target information needs to be extracted from the daytime noise by the polarization method in infrared band. This study develops a polarization bidirectional reflection distribution function while taking the ing function into consideration. It then validates the model's viability using parameter inversion, obtains the contrast between intensity imaging and polarization imaging through a model simulation of polarization angle and polarization degree, and validates the benefits of the polarization imaging technique for space targets.

2. Basic Theory of the Polarization Bidirectional Reflection Distribution Function Model

2.1. Bidirectional Reflection Distribution Function Model Based on Microplanes

The polarimetric scattering characteristics of surfaces can be completely described by the polarized bidirectional reflectance distribution function (pBRDF), which was defined by D.S. Flynn in 1995 [9].

While the actual surface of the object is rough, the actual normal z and the micro-surface normal do not coincide, and the size of the angle between the two lines can generally be thought of as meeting the Gaussian random distribution. This assumption forms the foundation of the traditional polarized bidirectional reflectance distribution function (pBRDF).

The probability density function for micro-surface elements $D(\omega)$ can be written as:

$$D(\omega) = \frac{1}{2\pi\sigma^2\cos^4\alpha}\exp(\frac{-\tan^2\alpha}{2\sigma^2}) \quad (1)$$

where σ is the coefficient of surface roughness of the object's material. The higher the value of σ, the closer the object's surface reflection is to diffuse reflection. As seen in Figure 1, $\boldsymbol{k}_i$ is the light wave vector that is incident, $\boldsymbol{k}_r$ is the light wave vector that is reflected, $\Delta\phi = \phi_{\mathrm{i}} - \phi_r$ is the relative azimuthal angle of the two light wave vectors, θ_i and θ_r are the angles of the incident light vector $\boldsymbol{k}_i$ and the reflected light vector $\boldsymbol{k}_r$ to the normal z, respectivelyz and n are the microplane and macroscopic normals of the rough material surface of the object with an α angle, and β is the angle between the light wave vectors that are incident and the microplane norm, where the following geometric relationship between α and β is satisfied.

$$\cos(2\beta) = \cos\theta_i\cos\theta_r + \sin\theta_i\sin\theta_r\cos\Delta\phi \quad (2)$$

$$\cos\alpha = \frac{\cos\theta_i + \cos\theta_r}{2\cos\beta} \quad (3)$$

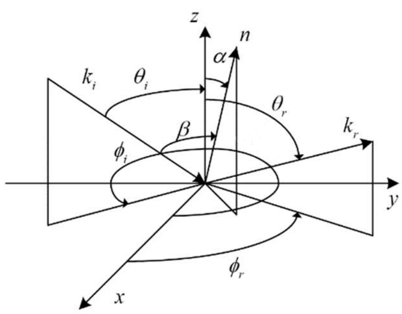

Figure 1. Angular relationship of the micro-surface model.

In order to continue to derive the geometric relationship between the angles within the microfacet element, the following two angles are introduced: The normal of the material's surface actually forms a plane with the incident light, as does the normal of the microplane element.

The incident light $\boldsymbol{k}_i$ forms a plane with the normal of the actual surface of the material, and also forms a plane with the normal of the microfacet. The included angle between the two surfaces is η_i, reflected light $\boldsymbol{k}_\text{r}$ forms η_r in the same way.

After calculation, we know that η_i, η_r, θ_i, θ_r, β satisfy the following equations:

$$\cos(\eta_i) = [(\cos\theta_i + \cos\theta_r)/(2\cos\beta) - \cos\theta_i\cos\beta]/(\sin\theta_i\sin\beta) \tag{4}$$

$$cos(\eta_r) = [(\cos\theta_i + \cos\theta_r)/(2\cos\beta) - \cos\theta_r\cos\beta]/(\sin\theta_r\sin\beta) \tag{5}$$

In the process of reflection on the surface of rough objects, there is also a partial scattering of light being blocked by the cutoff-masking phenomenon, which will affect the scattering characteristics of the reflected light. Accordingly, the expression of the specular scattering model of the micro-surface element bidirectional reflection distribution function taking the masking function into account is as follows:

$$f_{BRDF}(\theta_i, \phi_i, \theta_r, \phi_r, \lambda) = \frac{1}{2\pi}\frac{1}{4\sigma^2}\frac{1}{\cos^4\alpha}\frac{\exp\left[-\tan^2\alpha/2\sigma^2\right]}{\cos\theta_r\cos\theta_i}G(\theta_i, \phi_i, \theta_r, \phi_r) \tag{6}$$

where θ_i and θ_r are the angles of the incident and reflected light norm to the surface of the macroscopic object, respectively, and ϕ_i and ϕ_r are the horizontal azimuth angles of the incident and reflected light, respectively. $G(\theta_i, \phi_i, \theta_r, \phi_r)$ is the influence of the ing effect [10] effect from the masking effect.

Assuming $\phi_i = 0$, the shadowing function can be reduced to a function $G(\theta_i, \theta_r, \phi_r)$ with respect to $\theta, i\theta_r, \phi_r$, and the expression is derived using the approximation formula as follows [11]:

$$G(\theta_i, \theta_r, \phi_r) = \frac{1 + \frac{\omega_p\left|\tan\theta_{ip}\tan\theta_{rp}\right|}{1+\sigma_r\tan\beta_p}}{\left[(1+\omega_p\tan^2\theta_{ip})(1+\omega_p\tan^2\theta_{rp})\right]} \tag{7}$$

where the angle $\theta_{ip}, \theta_{rp}, \beta_p$ designates, in accordance with the following geometric relationships, the spherical projection of the angle $\theta_i, \theta_r, \beta$.

$$\begin{cases} \omega_p = \sigma_p(1 + \frac{u_p\sin\alpha}{\sin\alpha + v_p\cos\alpha}) \\ \tan\theta_{ip} = \tan\theta_i\frac{\sin\theta_i + \sin\theta_r\cos\varphi_r}{2\sin\alpha\cos\beta} \\ \tan\theta_{rp} = \tan\theta_r\frac{\sin\theta_r + \sin\theta_i\cos\varphi_r}{2\sin\alpha\cos\beta} \\ \tan\beta_p = \frac{|\cos\theta_i - \cos\beta|}{2\sin\alpha\cos\beta} \end{cases} \tag{8}$$

where σ_p, σ_r, u_p and v_p are empirical parameters connected to the surface-related material roughness coefficients and are often given the following empirical values [12]: $\sigma_p = 0.0136, \sigma_r = 0.0136, u_p = 9.0, v_p = 1.0$.

2.2. Multi-Parameter Polarization Bidirectional Reflection Distribution Function Model of Rough Material Surface

The bidirectional reflection distribution function can describe the reflection process of light rays on the surface of anisotropic objects more comprehensively. Not only the original intensity of the light will change, but so will its polarization state, and the polarization bidirectional reflection distribution function model is:

$$M(\theta_i, \phi_i; \theta_r, \phi_r; \lambda) = \frac{dL_r(\theta_i, \phi_i; \theta_r, \phi_r; \lambda)}{dE_i(\theta_i, \phi_i; \lambda)} \tag{9}$$

where dE_i and dL_r are the Stokes vectors of incident and scattered light.

Based on this, the polarization bidirectional reflection distribution function $M(\theta_i, \phi_i; \theta_r, \phi_r; \lambda)$ is created. This function is a crucial addition to the bidirectional reflection distribution function because it can reflect how the polarization state of light changes during the reflection process on an object's surface. The target's polarization characteristics can be determined using the polarization bidirectional reflection distribution function, and the algorithm can inverse the substance's fundamental physical properties.

Surface scattering and body scattering are the two main types of light scattered from material surfaces. This study assumes that body scattering and multiple scattering of light off rough material surfaces are both parts of the same non-polarized process and concurrently models and analyzes them.

The Mueller matrix [13], which may describe the scattering polarization characteristics of the target material, can be used to determine the relationship between the incident light and the scattered light Stokes vector using the polarization bi-directional reflection distribution function. In order to distinguish the effects brought on by the two scattered lights during the surface scattering of the material, the specular coefficient k_s is introduced in this paper, as well as a pBRDF model that includes the surface scattering component f_{sp} of the material.

$$f = f_{dd} + k_s f_{sp} \tag{10}$$

The body scattering component f_{dd} and the associated expressions, and ρ_d was proposed in the Le Hors work to elucidate the impact of body scattering in reflected light on the polarization state [14], as shown in following equations:

$$f_{dd_{i,j}} = \frac{\cos\theta_r}{\pi}\rho_d \cdot M^d_{i,j}(\theta_i, \theta_r, \Delta\phi, \eta) \tag{11}$$

$$\rho_d = (1 - R_i)\frac{(1 - k_2)R_\infty}{1 - k_2 R_\infty} \tag{12}$$

$$R_i = \frac{r_s + r_p}{2} \tag{13}$$

$M^d_{i,j}(\theta_i, \theta_r, \Delta\phi, \eta)$ is the Muller matrix of the body scattering effect, the Fresnel reflectance of the light that comes from the first medium and hits the target surface is known as R_i, which can be calculated from the Fresnel reflection coefficients r_s and r_p. k_2 represents the Fresnel reflectance of the scattered light that was incident on the target surface from the initial medium. R_∞ is the target surface's diffuse reflectance at roughly infinite thickness [15]. The expressions of r_s and r_p are shown as follows:

$$r_\mathrm{s} = \frac{(A - \cos\beta)^2 + B^2}{(A + \cos\beta)^2 + B^2} \tag{14}$$

$$r_p = r_s\frac{(A - \sin\beta\cos\beta)^2 + B^2}{(A + \sin\beta\cos\beta)^2 + B^2} \tag{15}$$

$$A = \sqrt{\frac{\sqrt{C} + D}{2}} \tag{16}$$

$$B = \sqrt{\frac{\sqrt{C} - D}{2}} \tag{17}$$

$$C = 4n^2k^2 + D^2 \tag{18}$$

$$D = n^2 - k^2 - \sin^2\beta \tag{19}$$

where n is the refractive index, and k is the absorption coefficient. $N = n + ik$ is the complex refractive index of the material. The refractive index n, defined as the ratio of the speed of light in a vacuum to the speed of light in a medium, reflects the degree of deflection of light as it travels through the medium. The extinction coefficient k is related to the exponential attenuation of light waves as they pass through the medium and can be thought of as representing the absorption of light by matter.

Based on the microsurface metatheory in Section 2.1 and considering the masking effect existing on the actual rough material surface, the representation of the surface scattering component f_{sp} is deduced as

$$f_{sp_{i,j}} = \frac{1}{8\pi\sigma^2\cos^4\alpha} \cdot \frac{\exp\left(\frac{\tan^2\alpha}{2\sigma^2}\right)}{\cos\theta_i\cos\theta_r} \cdot G(\theta_i, \theta_r, \Delta\phi) \cdot M_{i,j}(\theta_i, \theta_r, \Delta\phi; \eta) \tag{20}$$

where i, j denote the $i+1$ th row and $j+1$ th column in the Mueller matrix, and the value interval is an integer from 0 to 3; $\Delta\phi$ is the relative azimuth angle $\Delta\phi = \phi_i - \phi_r$; σ is the material surface roughness.

The Kubelka–Munk model was chosen to model the body scattering in the target scattered light [16,17], and the multiparametric polarization bi-directional reflection distribution function can be modeled by combining the surface scattering component f_{sp} expression and the body scattering component f_{dd} expression as

$$f_{i,j} = \frac{k_s}{8\pi\sigma^2\cos^4\alpha}\frac{\exp\left(-\frac{\tan^2\alpha}{2\sigma^2}\right)}{\cos\theta_i\cos\theta_r} \cdot G(\theta_i, \theta_r, \Delta\phi) \cdot M_{i,j}(\theta_i, \theta_r, \Delta\phi; \eta) + \frac{\cos\theta_r}{\pi}\rho_d \cdot M^d_{i,j}(\theta_i, \theta_r, \Delta\phi; \eta) \tag{21}$$

Since the circular polarization component in natural light is very small and negligible, its Stokes vector when natural light is incident can be expressed as $E_i = [100]^T$, and consequently the Stokes vector of the reflected light is as in Equation (22):

$$L_r = \begin{bmatrix} f_{sp_{00}} f_{sp_{01}} f_{sp_{02}} \\ f_{sp_{10}} f_{sp_{11}} f_{sp_{12}} \\ f_{sp_{20}} f_{sp_{21}} f_{sp_{22}} \end{bmatrix} \begin{bmatrix} 1 \\ 0 \\ 0 \end{bmatrix} = \begin{bmatrix} f_{sp_{00}} \\ f_{sp_{10}} \\ f_{sp_{20}} \end{bmatrix} \tag{22}$$

where L_r is the reflected irradiance Stokes vector parameter and $f_{i,j}$ is the pBRDF Mueller matrix element. Assuming that the radiation incident on the material surface is unpolarized natural light, the polarization of the scattered light is known as DOP. The expression of polarization can then be deduced as:

$$DOP = \frac{\sqrt{\left(k_s f_{sp_{0,0}}\right)^2 + \left(k_s f_{sp_{2,0}}\right)^2}}{k_s f_{sp_{0,0}}} = \frac{\frac{k_s}{16\pi\sigma^2\cos^4\alpha} \cdot \frac{\exp\left(-\frac{\tan^2\alpha}{2\sigma^2}\right)}{\cos\theta_i\cos\theta_r} \cdot G\left(r_s - r_p\right)}{\frac{k_s}{16\pi\sigma^2\cos^4\alpha} \cdot \frac{\exp\left(-\frac{\tan^2\alpha}{2\sigma^2}\right)}{\cos\theta_i\cos\theta_r} \cdot G\left(r_s + r_p\right) + \frac{\cos\theta_r}{\pi}\rho_d} \tag{23}$$

As can be seen from the Formulas (19) and (23), the polarization value of a rough surface material is determined by five physical characteristics of the material, namely n, k, σ, k_s, and ρ_d. The degree of polarization and other information about the target material are typically directly obtained by polarization imaging. Experiments cannot be used to directly measure the five aforementioned parameters. In order to generate the five physical parameters needed for the model, this research will use methods to invert the degree of polarization information obtained from experiments.

2.3. Parametric Genetic Algorithm Inversion Verification

In this paper, a genetic algorithm is selected to invert five key unknown parameters in the model, denoted as a_1, a_2, a_3, a_4 and a_5. The basic parameters and operations of the genetic algorithm are set and selected for the needs of this paper as follows.

Step 1: Create an initial population of chromosomes encoded by genes at random. We use universal binary coding in this paper and assume that the range of individual a values to be inverted is $[a_{\min}, a_{\max}]$, so the binary number of nnn bits b is

$$b = \frac{(2^n - 1)(a - a_{\min})}{(a_{\max} - a_{\min})} \tag{24}$$

The first-generation initial population consists of all the individuals compiled using the adopted coding at the very beginning, where the genes on the individuals in the initial population are usually generated randomly within their range of values. In this paper, we set the initial population size to 100 randomly generated individuals.

Step 2: Calculate the fitness function value for each chromosome, end the loop iteration by satisfying the output condition, and output the optimal five covariates after decoding;

if the output condition is not satisfied, continue to run down. In this paper, the fitness function is chosen as the standard mean squared deviation model of the simulated value k and the experimentally measured polarization value n, to ensure the trend of selecting individuals during the selection process.

$$f(n,k,\sigma,k_s,\rho) = \frac{\sum_{\theta_i}(P' - P)^2}{\sum_{\theta_i}(P)^2} \tag{25}$$

Step 3: The $100 - N$ individuals with relatively good fitness functions are chosen to form a new population. In the new population, the set crossover probability and method operation are run In the selected population, there is a chance that two individuals are randomly chosen to exchange the same type of inverse covariates, which is known as the crossover operation in the genetic algorithm. In other words, two new chromosomes are formed by swapping alleles from a randomly paired pair of chromosomes. The crossover chance is set to 0.02, and single-point, multi-point, and uniform crossover methods can all occur at the same time.

Step 4: The set mutation probability and method operations are run in the new population; the inverse covariates in the population's individuals are all given a certain probability to revalue in the range of values to produce a new individual, which is called the mutation operation in the genetic algorithm, i.e., the genes on the chromosome mutate to other alleles with a certain probability to produce a new chromosome. The mutation probability is 0.02, and uniform, boundary, and basic position mutations can all occur at the same time.

Step 5: The population is run again in step 2 after selection, crossover, and mutation. When the output condition is met, the population genetic iteration is terminated. The output condition is that the difference in fitness function between the largest individual in the population and the average fitness function of all individuals in the population is less than 10^{-3}, and the algorithm's maximum number of inheritance N cannot exceed 100.

In order to verify the reliability of the theoretical model, the polarization measurements in the literature [18] are used to invert the parameters of complex refractive index N, specularity coefficient k_s and reflectivity parameter ρ_d of aluminum and black lacquer materials, and the inversion results are obtained and compared with the reference literature to obtain the error values.

The complex refractive index of the material is $N = n + ki$, where n is the refractive index and k is the absorption coefficient, both of which are wavelength-dependent.

The inversion results of the two materials after the genetic algorithm operation are shown in Table 1, and it can be seen that the results of the inversion of the complex refractive index of the two materials are closer to the real values than those of the reference literature [18].

Table 1. Inversion results of complex refractive index of aluminum and black paint materials.

Materials	Truth		Reference		Estimated	
	n	k	n	k	n	k
Aluminum	1.24	6.6	1.37	3.97	1.231	6.574
Black Paint	1.405	0.2289	1.46	1.32	1.429	0.2398

The inverse material parameters are substituted into the multi-parameter model of this paper and the Torrance-Sparrow model [19] to verify the accuracy of the multi-parameter model, and the simulation curves of the reflected light polarization of the two materials under the two models vary with the angle of the incident zenith of the light source are obtained, and the DOP simulation curves of the materials are compared with the experimental data. Figure 2 depicts this. The results show that the actual surface of the material is not perfectly smooth, and there is also a scattering phenomenon of body scattering in addition to specular reflection of light on the surface of the material, and the body scattering is characterized by a deflection effect, which causes the simulation polarization value of the two materials to be low overall, so the simulation curve of the multi-parameter model in this paper is more consistent with the experiment.

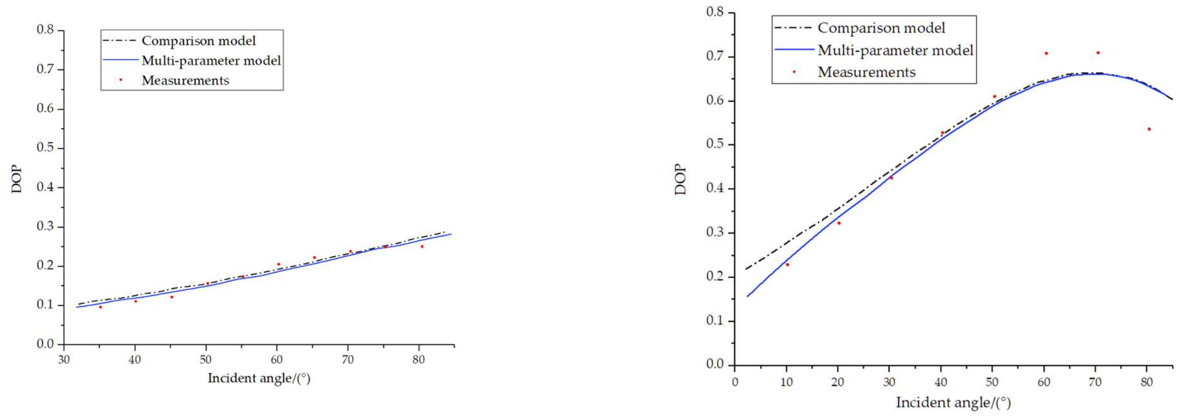

(**a**) (**b**)

Figure 2. DOP simulation curves of materials under different models, (**a**) Aluminum. (**b**) Black paint materials.

3. Characteristics of the Sky Background Polarization Distribution

3.1. Establishment of Rayleigh Scattering Model for Sky Background Polarization

The sun position affects the sky background polarization distribution characteristics, and in order to introduce the relationship between the ground-based optical system and the sun position, thehorizontal coordinate system is used. A schematic diagram of the horizontalcoordinate system is shown in Figure 3, which can be obtained from the vertical projection of the celestial coordinate system in the equatorial plane. The position of the Sun is S_1, the position of the ground-based optical system is O, the plane where the optical system is located is XOY, and OV is the direction of the space target detected by the ground-based optical system, which intersects with the celestial sphere at point V. The altitude angle and azimuth angle of the Sun are θ_S and φ_s, respectively, and the altitude angle and azimuth angle of the space target detected by the ground-based optical system can be expressed by θ and φ, respectively. South, north, east and west directions are replaced by S, N, E, and W respectively.

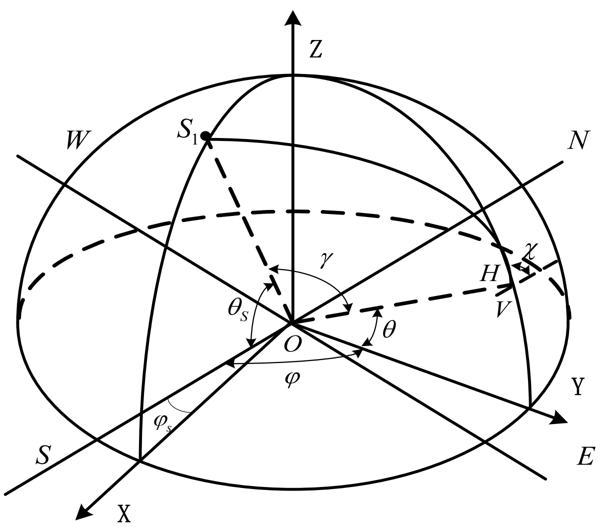

Figure 3. Horizontal coordinate system diagram.

According to the study of the Rayleigh scattering process in this paper, the scattering plane in the geodetic coordinate system is the plane where SOV is located, the scattering angle γ is the angle between the ground-based optical system and the sun line OS and the ground-based optical system detection direction OV, and the polarization angle can be expressed by $\chi = 90^\circ - \angle ZVS$.

According to the cosine theorem of spherical triangles, the scattering angle can be derived to satisfy the following geometric relations:

$$\cos\gamma = \cos\left(\frac{\pi}{2} - \theta\right)\cos\left(\frac{\pi}{2} - \theta_S\right) + \sin\left(\frac{\pi}{2} - \theta\right)\sin\left(\frac{\pi}{2} - \theta_S\right)\cos(\varphi - \varphi_S) \quad (26)$$

The result is:

$$\cos\gamma = \sin\theta\sin\theta_S + \cos\theta\cos\theta_S\cos(\varphi - \varphi_S) \quad (27)$$

The expression can be derived from the basic definition of the polarization degree as follows:

$$P = P_{\max}\left(\frac{1 - \cos^2\gamma}{1 + \cos^2\gamma}\right) \quad (28)$$

where, the $P_{\max}$ maximum polarization of the sky background is the maximum, and the presence of fully polarized light in the sky background light is 1.

Before finding the polarization angle expression, it is necessary to derive the expression $R(r,\theta,\varphi)$ of the sunlight vector at the space position according to Rayleigh e scattering law as follows:

$$e = v\cos\chi + h\sin\chi \quad (29)$$

where, $\mathrm{v} = -(\cos\theta\cos\varphi, -\cos\theta\sin\varphi, \sin\theta)$, $h = (-\sin\varphi, \cos\varphi, 0)$, r, θ, and φ are the coordinate components of the target in the ground level coordinate system. The expression of the space object polarization angle information χ at the $R(r,\theta,\varphi)$ ground level coordinates is derived by setting the ground level coordinates of the Sun S to (r,θ_S,φ_S).

$$\tan\chi = \frac{\sin\theta\cos\theta_S - \cos\theta\sin\theta_S\cos(\varphi - \varphi_S)}{\sin(\varphi - \varphi_S)\sin\theta_S} \quad (30)$$

3.2. Sky Background Polarization Scattering Model Complex Spherical Projection Representation

According to the polarization degree and polarization angle formula, the polarization information at any position in the sky background in the three-dimensional horizon coordinate system can be treated by the pseudo-color algorithm to distinguish the polarization information differences in different locations. In order to make the results of this study generalizable, the three-dimensional polarization distribution is projected into a two-dimensional polarization distribution. Figures 4 and 5 are the simulation results of the model under the conditions of 0° solar altitude and azimuth.

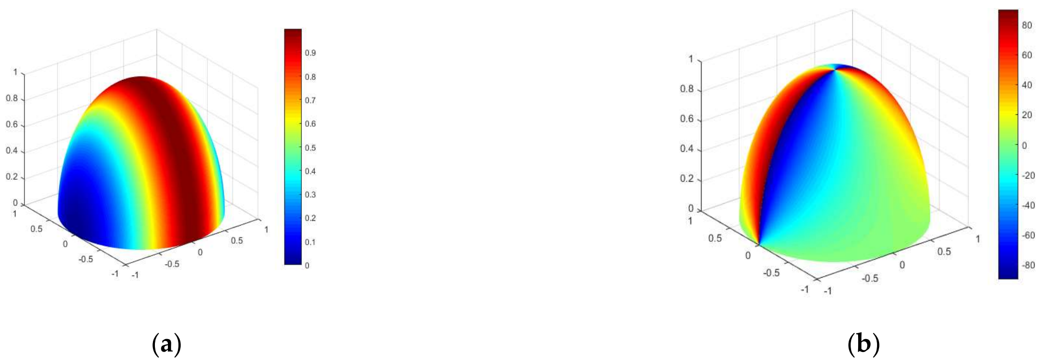

Figure 4. 3–D polarization distribution characteristics of Rayleigh scattering sky background, (**a**) Polarization degree (**b**) Polarization angle.

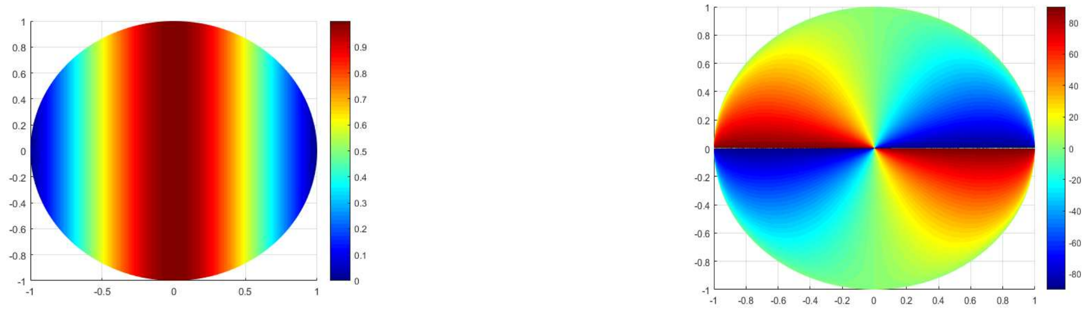

(a)

(b)

Figure 5. Polarization distribution characteristics of 2–D vertical projection of Rayleigh scattering, (**a**) Polarization degree (**b**) Polarization angle.

The direct vertical projection method is commonly used to convert the three-dimensional polarization distribution of the simulated sky background into a two-dimensional distribution. However, the projection method lacks a rigorous correspondence, resulting in information loss, which cannot be reverse projected, and also makes the proportion of the zenith area greater than the actual distribution.

In this paper, the polarization distribution characteristics of the sky background theory are expressed using the complex spherical mapping theory, which effectively solves the problem of losing polarization information during direct vertical projection [17].

Each location on the celestial sphere can be projected to the point on the plane where the optical system is placed, according to the theory of complex spherical mapping. At this point, the sophisticated spherical projection-based two-dimensional polarization distribution model of the sky background can be constructed. Figure 6 depicts the complex sphere's particular projection method. The complex sphere $Z = R$ establishes the $x_m o_m y_m$ coordinate system by using $(0, 0, r)$ as the coordinate origin. L is the line formed by joining any two points $R(x_0, y_0, z_0)$ and $z'(0, 0, -r)$ on the celestial sphere E. Because the normal of complex sphere $z = r$ is not orthogonal to the line L, the complex sphere $z = r$ must meet the line L at $R_m(x_m, y_m)$. According to the complex sphere mapping theory, each point on the celestial sphere E can be projected onto the complex sphere $z = r$ using the above technique.

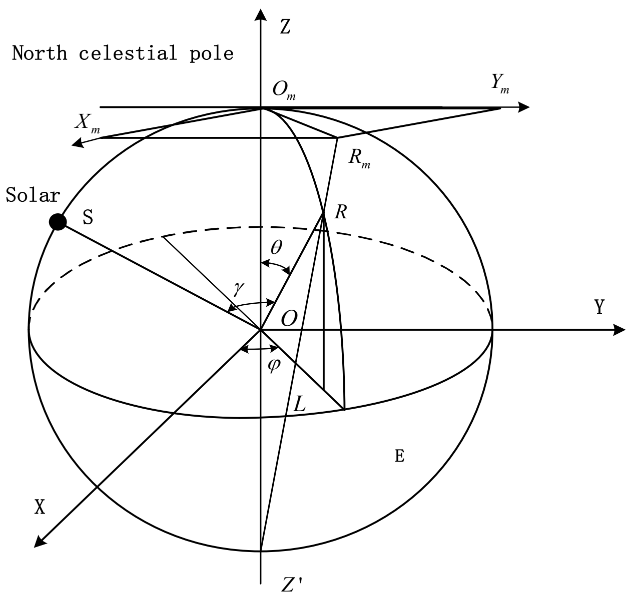

Figure 6. Complex sphere mapping relation diagram.

In a coordinate system $oxyz$, a complex spherical coordinate system $x_m o y_m$ is represented as:

$$z = r \tag{31}$$

The equation for a straight line L is expressed as:

$$\frac{x}{x_0} = \frac{y}{y_0} = \frac{z + r}{z_0 + r} \tag{32}$$

When actually imaging the foundation of a space target, it is only necessary to consider the impact of the sky background in hemispherical space. Therefore, it can be deduced from the spatial geometry that any point $R(r, \theta, \varphi)$ in the hemisphere space on the celestial sphere E corresponds to the coordinates of the points $R_m(x_m, y_m)$ projected onto the complex sphere.

Since only the influence of the sky background in the hemispheric space needs to be considered when actually performing ground-based detection imaging of space targets. Therefore, the coordinates of the point $R(r, \theta, \varphi)$ corresponding to the projection of any point $R_m(x_m, y_m)$ in hemispheric space on the celestial sphere E onto the complex sphere $z = r$ can be deduced from the spatial geometric relations as Equation (33):

$$x_m + i y_m = 2r \tan(\theta/2) \exp(i\varphi) \tag{33}$$

In summary, a two-dimensional polarization distribution model of the sky background based on the complex spherical projection theory can be established. The comparison of this model with the simulation effect of the model using direct vertical projection is shown in Figures 5 and 7. It can be found that the model using complex spherical projection derived in this section can effectively correct the aberrations caused by the direct vertical projection method, and the percentage of the zenith region has been reduced to a certain extent.

(**a**) (**b**)

Figure 7. 2–D polarization distribution characteristics of sky complex spherical projection, (**a**) Polarization degree (**b**) Polarization angle.

4. Imaging Contrast Simulation Analysis

Simulation work was carried out for the National Astronomical Observatory of the Chinese Academy of Sciences Changchun Satellite Observatory (43°8′ N, 125°32′ E) on 16 December 2020, at 11:42 a.m. under specific space target relative position conditions, where the solar zenith angle θ_o and azimuth angle are 29°30′ and −04°32′, respectively. Based on the simulation work, the analysis of the effect of ground-based polarization imaging of the space target in this paper will be continued with the following settings.

As shown in Figure 8, it is assumed that the polyimide film, solar panel, aluminum plate and #54 black backplane are on the same flat plate, in the same plane with the sun and the ground-based optical system, and the relative azimuth of the sun and the ground-based optical system and the space target in this plane is 180°.

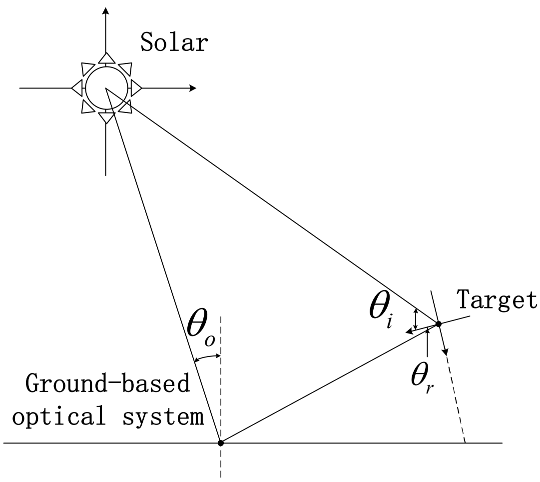

Figure 8. Geometric angle diagram of the detection time of the space target on the ground.

The sun is at 180° relative azimuth to both the space target and the ground-based optical system. The sun is regarded to be a parallel light source, and the incident parallel light angle θ_i on the surface of the space target is set to 30° in this paper, and the ground-based polarization imaging effect of the satellite observation angle θ_r under different altitude angle conditions is analyzed under the above conditions.

The simulation of polarization of four materials, namely polyimide film, solar panel, aluminum panel and #54 black backsheet, is carried out first. By substituting the above conditions $\theta_i = 30°$, $\Delta\phi = 180°$ and the physical parameters of the materials obtained by inversion into the pBRDF model established in this paper, the relationship of θ_r and their degree of polarization can be obtained, as shown in Figure 9.

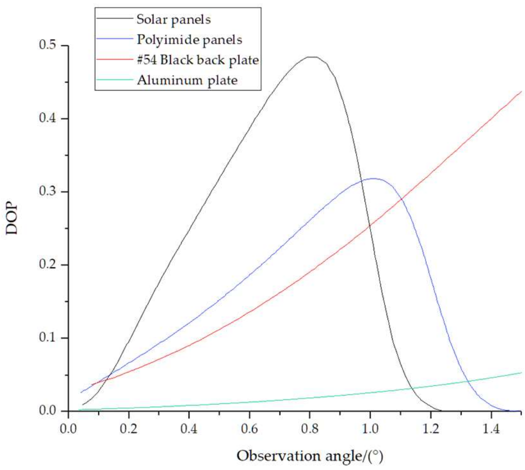

Figure 9. The relationship of DOP and θ_r of four satellite surface materials.

Next, the solar zenith angle θ_o = 29°30′ and azimuth angle −04°32′, the space target azimuth angle 101°28′ is substituted into the sky background Rayleigh scattering model, and the simulation of the sky background polarization value under this condition can be obtained as follows:

In Figure 10, B represents the Babinet neutral point, O_m represents the zenith center of the sky, and the black line represents the plane including the Sun, the ground-based optical system, and the space target. The distribution curve of the polarization value of the sky background of the space target with the zenith angle into the relative azimuth of the sun is represented by the line segment over O_m and the sun, from which we can obtain the polarization value of the sky background of the space target at any zenith angle at this time, and the space targets at 10° and 60° zenith angles are analyzed and discussed in this paper.

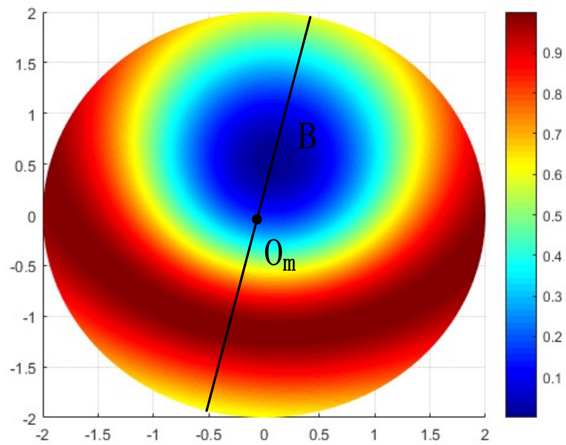

Figure 10. Simulation of the polarization value of the sky background.

After the target is irradiated by sunlight, the spherical scattering model simulation is used, and assuming that the incident light is completely passed by polarized light radiation and half of the unpolarized radiation is transmitted, the luminous flux arriving at the pupil is deduced as:

$$\Phi_s = \frac{I_s \cdot \lambda}{L^2 \cdot h \cdot c} = \frac{1.65R^2 \cdot \rho_0 \cdot (1 + P_s) \cdot [(\pi - \phi)\cos\phi + \sin\phi]}{\pi L^2} (\text{photons}/\left(\text{m}^2 \cdot \text{s}\right)) \quad (34)$$

where, P_s is the polarization of the space target, ρ_0 is the average reflectivity of the target in the detection band, L is the space target orbit height, Planck's constant is h, c is the speed of light, λ is the detection of the central band of the working band, and ϕ is the scattered light phase angle, set the band for 1.5~1.8 μm. When the signal detection effectiveness is guaranteed that the SNR is 6, the minimum imaging luminous flux of space target for ground-based optical system polarization imaging is estimated to be $\Phi_s = 8.472 \times 10^5 \text{photons}/\left(\text{m}^2 \cdot \text{s}\right)$.

The expression of the number of electrons of the space target on the target surface of the system detector is as Equation (35) shows, the parameters are show in Table 2.

$$N_s = \frac{1}{\boldsymbol{k}} \cdot \Phi_s \cdot A_0 \cdot \tau_0 \cdot \tau_s \cdot \tau_p \cdot Q_B \cdot t_s \cdot \left(1 - \varepsilon^2\right) \cdot f_s \quad (35)$$

Table 2. The parameter, definition and value of Equation (35).

	Definition	
k	number of image elements occupied by the image spot on the detector target surface	4
A_0	system pupil area	2.544 m^2
τ_0	system transmittance	0.9
τ_s	average atmospheric transmittance in the operating band range	0.7
τ_p	average transmittance of the micropolarizer array of the polarization device in front of the image elements occupied by the target	0.7
Q_B	average quantum efficiency of the detector for the effective signal	0.65
t_s	integration time of the detector to collect the space target information	0.025 s
ε	blocking ratio existing in the structure of the card-based system	0.2
f_s	transmittance coefficient of the reflected light from the space target by the spectral filter	0.13

Similarly, the expression of the number of photoelectrons that can obtain the sky background signal that reaches the detector target in the real-time imaging method of the micropolar array is:

$$N_B = \Phi_B \cdot A_0 \cdot \tau_0 \cdot \tau_p \cdot Q_B \cdot t_B \cdot f_B \cdot A_p^2 \cdot \left(1 - \varepsilon^2\right) \cdot \frac{1 + P_B}{2} \quad (36)$$

where $\Phi_B = 5.6 \cdot 10^{10}/2.512^{M_B}$ is the number of background-generated photons, M_B is the deep-sky background equivalent magnitude, which is 22, and $t_B = 0.025s$ is the integration time for the detector to collect the spatial target information, $f_B = 0.021$ is the transmittance coefficient of the filter for the sky background noise, $A_P = d_{pix}/f' = 0.047''$ is the instantaneous field of view of a single image element of the detector, $d_{pix} = 15$ μm is the image element size of the detector and f' is the system focal length.

In the case, P_B is the polarization of the sky background. Considering the photon noise caused by the target and the sky background, the total noise signal expression of the system is:

$$N = \sqrt{N_s + N_B + N_D \cdot t_s \cdot k + N_R^2} \tag{37}$$

where $N_D = 0.183e^-$ is the dark current noise of a single pixel of the detector, t_s is the integration time of the detector, $N_R = 60e^-$ is the readout noise of the detector. Finally, the detection signal-to-noise ratio expression can be derived as:

$$SNR = \frac{N_s}{N} \tag{38}$$

The system's limit detection capability will be expressed in the concept of star magnitude, and its transformation relationship is:

$$M = 2.5 \log\left(\frac{\int_{\lambda_1}^{\lambda_2} \frac{1}{{T_0}^4 \cdot \lambda^4} \cdot \frac{8.48 \times 10^{34} \times 10^{-0.4bc}}{e^{(1.44 \times 10^8/\lambda T_0)} - 1} d\lambda}{\Phi_s} \right) \tag{39}$$

where T_0 is the stellar equivalent temperature, and bc is the bolometric correction, bc takes 0.08, and T_0 is 5900 K.

Let the target be at the orbit radius of 500 km with the same distribution of sky background in the field of view. By substituting the zenith angle and azimuth angle of the space target (A = 10°, E = 101°28′ and A = 60°, E = 10°8′, respectively) into the complex spherical coordinate system, the polarization value P_B of the space target surface material can be found in Figure 9, and the corresponding sky background polarization value P_s can be obtained from Figure 10. Referring to Equation (38), we know the range of the ultimate imaging capability of the system, the range of the target-background contrast of the original intensity imaging under the ultimate detection conditions, and the range of the target-background contrast in the polarization degree image obtained by the polarization imaging technique. The calculation results are shown in Table 3.

Table 3. Contrast calculation result.

	Polarization Value	Extreme Imaging Capability Range	Raw Intensity Imaging Contrast	Polarization Imaging Contrast
A = 10°, E = 101°28′	0.32	[8.86, 9.28]	[0.028, 0.042]	[0.006, 1.5]
A = 60°, E = 101°28′	0.89	[8.83, 9.23]	[0.029, 0.043]	[0.002, 0.539]

When the system reaches the limit of detection capability, the space target brightness and sky background brightness difference of 3~4 magnitude, the brightness of the sky background is generally 15.85~39.82 times the brightness of the space target, when the signal-to-noise ratio is greater than 6, the detector can be considered corresponding, but the effective signal under this condition is susceptible to background noise interference, imaging contrast is extremely poor.

The polarization technology, by acquiring the polarization image of the space target and the sky background, converts the contrast between the sky background and the space target from a value with a large difference in magnitude to a value with the same magnitude at certain angles, so that the system can greatly improve the target-background contrast index at a certain detection angle when detecting the space target with a weak signal-to-noise ratio.

For example, the polarization of the polyimide plate can reach about 0.48 when the macroscopic surface normal of the polyimide plate is at an angle of 62° from the center of the field of view of the ground-based optical system at a position of 10° zenith angle and 101°28′ azimuth angle, while the polarization of the sky background is only 0.32.

Sometimes, the polarization contrast will indeed be lower than the contrast of intensity imaging due to the low brightness of the polarized image caused by the addition of a micropolarizer array, but a higher contrast of polarized imaging can be obtained by choosing the most appropriate satellite observation angle. The highest value of spatial target-background contrast can reach 1.5, which is improved by 35.71 times compared to the maximum value of target-background contrast of 0.042 for the original intensity imaging technique at this condition.

At this time, the target pixel value in the polarization image acquired by the system is larger than the value of the bright sky background, which effectively reflects and uses the ability of polarization imaging technology to "weaken strong light" and "strengthen weak light", so that the weak space object signal is highlighted in the strong background noise of the daytime sky.

In summary, the space target polarization imaging technology can greatly improve the target-background contrast index under certain angles. The difference between space target and sky background polarization characteristics can be used to capture space targets more efficiently in the stable sky background polarization distribution, which can effectively solve the problem of low imaging contrast caused by strong background noise interference during daytime, and can become an important technical component of the all-day space target ground-based observation network.

5. Conclusions

In this paper, based on the traditional BRDF model, considering that the normal of the rough surface and the normal of the microsurface element do not coincide, a microsurface element BRDF model considering the masking function is established, and a pBRDF model is further established. Aluminum and black paint are selected, and the physical parameters in the model are verified by genetic algorithm inversion, and it is found that the model in this paper is closer to the real value than the reference literature model. The astronomical coordinate system and the geodetic coordinate system are introduced to study the sky background polarization distribution characteristics, and the space object polarization angle information is derived according to the Rayleigh scattering law. A complex spherical projection is used to project the background polarization from 3–D to 2–D, which has less aberration. The target-background contrast values of the original intensity and the polarization intensity are obtained by selecting the zenith angles of 10° and 60° and their azimuth angles, respectively. The polarization method is found to be significantly higher than the original intensity method.

Author Contributions: Data curation, H.C.; Formal analysis, H.C. and Q.F.; Funding acquisition, Q.F. and Y.L.; Methodology, Q.F.; Project administration, Q.F.; Resources, Q.F. and F.Z.; Supervision, Q.F.; Writing—original draft, H.C.; Writing—review and editing, F.Z. and R.Z. All authors have read and agreed to the published version of the manuscript.

Funding: This research was funded by Changchun University of Science and Technology, China. Huilin Jiang, National Natural Science Foundation of China, grant number 61890963.

Institutional Review Board Statement: Not applicable.

Informed Consent Statement: Not applicable.

Data Availability Statement: The study did not report any data.

Conflicts of Interest: The authors declare no conflict of interest.

References

1. Jiang, H.L.; Fu, Q.; Zhang, Y.L.; Jiang, L. Discussion on integrated technology of space debris laser detection, imaging and communication. *Infrared Laser Eng.* **2016**, *45*, 7.
2. Xu, M.; Shi, H.D.; Wang, C.; Liu, Z.; Fu, Q.; Ying Chao, L.; Dong, K.Y.; Jiang, H.L. Research on the integration technology of multi-dimensional space target detection and laser communication. *Chin. J. Lasers* **2021**, *48*, 223–235.
3. Zhang, Y.L.; Fu, Q.; Jiang, H.L.; Wang, C.; Han, L. Parameter analysis of range imaging communication integrated optical system. *Chin. J. Lasers* **2017**, *44*, 206–212.
4. Jiang, H.L.; Jiang, L.; Fu, Q.; Dong, K.Y. Research on space debris polarization spectral imaging detection technology. *J. Deep. Space Explor.* **2015**, 272–277. [CrossRef]
5. Shi, X.W.; Xu, X.J. Detector material and sensitivity analysis for space-based infrared sensors. *Optoelectron. Lett.* **2010**, *6*, 27–30. [CrossRef]
6. Jorgensen, K.; Africano, J.L.; Stansbery, E.G.; Kervin, P.W.; Hamada, K.M.; Sydney, P.F.; Pirich, A.R.; Repak, P.L.; Idell, P.S.; Czyzak, S.R. Determining the material type of man-made orbiting objects using low-resolution reflectance spectroscopy. *Int. Soc. Opt. Photonics* **2001**, *4490*, 237–244.
7. Ratliff, B.M.; Lemaster, D.A.; Mack, R.T.; Villeneuve, P.V.; Weinheimer, J.J.; Middendorf, J.R. Detection and tracking of RC model aircraft in LWIR microgrid polarimeter data. In Proceedings of the Polarization Science and Remote Sensing V, San Diego, CA, USA, 9 September 2011; pp. 29–41.
8. Namer, E.; Shwartz, S.; Schechner, Y.Y. Skyless polarimetric calibration and visibility enhancement. *Opt. Express* **2009**, *17*, 472–493. [CrossRef] [PubMed]
9. Flynn, D.S.; Alexander, C. Polarized surface scattering expressed in terms of a bidirectional reflectance distribution function matrix. *Opt. Eng.* **1995**, *34*, 1646–1650.
10. Blinn, J.F. Models of light reflection for computer synthesized pictures. In Proceedings of the 4th Annual Conference on Computer Graphics and Interactive Techniques, San Jose, CA, USA, 20–22 July 1977; pp. 192–198.
11. Meng, Q.Y.; Zhang, W.; Long, F.N. Analysis on the Detection Ability of Visible Cameras for Space based Space Targets. *Infrared Laser Eng.* **2012**, *41*, 6.
12. Huang, C.J.; Liu, Y.F.; Yin, J.W.; Sun, Y.Q.; Long, S.M. Inversion of Target Surface Masking Function Parameters and Optimization of BRDF Statistical Modeling. *Infrared Laser Eng.* **2010**, *39*, 883–886+891.
13. Gong, L.; Pan, Y.Q.; Wu, Z.S. Study on orientation diagnosis of Rayleigh defect particles in optical surfaces by light scattering characteristics. *Acta Photonica Sin.* **2014**, *43*, 831003. [CrossRef]
14. Le Hors, L.; Hartemann, P.; Dolfi, D.; Breugnot, S. Phenomenological model of paints for multispectral polarimetric imaging. In Proceedings of the Spie the International Society for Optical Engineering, Newton, MA, USA, 31 October–1 November 2001; p. 4370.
15. Saunderson, J.L. Calculation of the Color of Pigmented Plastics. *J. Opt. Soc. Am.* **1942**, *32*, 727–729. [CrossRef]
16. Li, J.W. *Infrared Polarization Imaging Technology and Application*; Science Press: Beijing, China, 2017.
17. Murphy, A.B. Modified Kubelka-Munk model for calculation of the reflectance of coatings with optically-rough surfaces. *J. Phys. D Appl. Phys.* **2006**, *39*, 3571. [CrossRef]
18. Yang, Y.F.; Wu, Z.S.; Cao, Y.H. Practical six-parameter bidirectional reflectance distribution functionmodel for rough surfaces. *Opt. Eng.* **2012**, *32*, 306–311.
19. Liu, Y. Design of Infrared Imaging Optical System for Space-Based Space Targets Based on Micro Polarization. Master's Thesis, Changchun University of Science and Technology, Changchun, China, 2020.